Oblique shocks in shallow flows of power-law fluids past abrupt channel deviations – Supplementary material

Andrea Baroni[1], Michele Iervolino[2], Luca Chiapponi[3], Cristiana Di Cristo[4], Andrea Vacca[4], Sandro Longo[3] and Vittorio Di Federico[1]

[1]Department of Civil, Chemical, Environmental and Materials Engineering, Alma Mater Studiorum Università di Bologna, Bologna, Italy

[2]Department of Engineering, Università degli Studi della Campania 'L. Vanvitelli', Aversa (CE), Italy

[3]Department of Engineering and Architecture - Università degli Studi di Parma - Parco Area delle Scienze 181/A - 43124 Parma - Italy

[4]Department of Civil, Building and Environmental Engineering, Università degli Studi di Napoli 'Federico II', Napoli, Italy

(Received xx; revised xx; accepted xx)

1. Experimental set-up

The design of the experimental setup was informed by preliminary tests carried out in a fully confined configuration, in which two channels of equal width were connected at a prescribed angle. These tests showed that the presence of a downstream confining wall strengthens the rarefaction wave originating from the inner corner, thereby reducing the distance available for measuring the shock properties. Although the flow may locally exhibit two-dimensional features near the jump, several recordings clearly indicate that it remains self-confined and predominantly one-dimensional. For this reason, only the upstream (feed) channel was confined. In addition, the analytical models assume a one-dimensional flow in channels of effectively infinite width, so a configuration with two confining channels would not be fully consistent with their underlying hypotheses. These preliminary experiments therefore justified the adopted experimental arrangement.

The illumination of the test section was provided from below by a highly uniform LED source. The channel inlet consisted of a converging section with a rectangular outlet that corresponded to the channel width and a height ranging from 2 to 5 mm, with the lower height used for shear-thickening fluids. The recirculation system included a vane pump regulated by an inverter and a measurement setup incorporating a magnetic flow meter. During preliminary long-duration tests, the fluid temperature was observed to increase significantly above ambient, as measured by a thermocouple immersed in the feed tank. To mitigate excessive temperature variations, a heat exchanger connected to a thermostat-controlled chiller was installed in the tank.

Fluid level measurements were performed using two Banner ultrasonic distance sensors, each with a nominal accuracy of 0.3 mm and a sampling frequency of 100 Hz. Qualitative information on water level was also inferred from the intensity of fluid coloration, which increases with fluid depth.

Abstract must not spill onto p.2

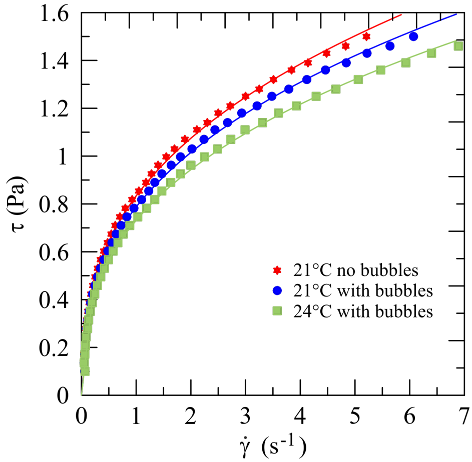

Figure 1: Rheometric curves of shear stress versus shear rate for the shear-thinning fluid at 21 °C both with and without bubbles, and at 24 °C with bubbles. Solid lines denote the fitted power-law models.

The depth of the upstream current before the jump, Y_1, was measurable in all cases and remained close to the height of 5 mm of the outlet section. However, measurement of the depth of the downstream current , Y_2, was only possible when the jump width perpendicular to the inclined wall was sufficient to reflect the ultrasonic waves. Furthermore, the local curvature of the fluid surface had to be limited to ensure a detectable echo. Consequently, Y_2 could not be obtained in certain experiments.

The experiments involved fluids exhibiting different rheological behaviors to investigate their influence on flow characteristics. The non-Newtonian shear-thinning fluid was prepared by mixing water and glycerol with varying concentrations of Xanthan gum, achieving a sufficiently low flow behavior index to enhance sensitivity to rheological effects. To retard biochemical degradation, a biocide was added in controlled amounts, while food coloring was included to improve the optical absorption properties of the fluid.

The non-Newtonian shear-thickening fluid consisted of a suspension of corn starch in a salt solution (potassium hydrogen phosphate, K_2HPO_4) mixed with water (900 g of salt per liter), resulting in a density of 1563 kg m^{-3} to prevent sedimentation. The high salt concentration also inhibited biodegradation, ensuring the stability of the mixture.

The Newtonian fluid was composed of water and glycerol, with an increased viscosity to maintain laminar flow conditions.

Rheological measurements of the shear-thinning fluid were conducted using an Anton Paar MCR101 rheometer equipped with a 25 mm parallel-plate geometry and a 1 mm gap. A notable feature was the high concentration of entrained air bubbles, attributed to high flow velocities. Because complete bubble removal proved challenging, the fluid-air mixture was taken into account in both density and rheological characterizations. The presence of bubbles was found to improve the shear-thinning behavior, as demonstrated in Figure 1, which compares the measurements of the same fluid with and without bubbles in 21 °C, and with bubbles at 24 °C.

Rheological measurements of the shear-thickening fluid were performed using an Anton Paar MCR702 TwinDrive rheometer with concentric cylinders operating in Couette flow (stationary inner cylinder and rotating outer cylinder). The tests were performed at various temperatures within the high shear-rate regime, which is representative of conditions in the flow field. Due to the relatively high apparent viscosity of the fluid and the consequent viscous dissipation, the thermostatic control system could not maintain a constant temperature, requiring tests in the range 25–30 °C. Figure 2(a) presents the rheometric curves for the shear-thickening fluid, while Figure 2(b) shows the temperature dependence of the fluid behaviour index and the consistency index, respectively. The values adopted to analyze the results reflect the different temperatures measured during the tests.

It should be noted that all rheometric curves display a distinct discontinuity at approximately $\dot{\gamma} \approx 20\,\mathrm{s}^{-1}$. Beyond this point, the curves reestablish a nearly constant slope, which varies only slightly and remains consistently greater than unity, indicating persistent shear-thickening behaviour. This discontinuity likely corresponds to a transition in the microstructural dynamics of the suspension, such as particle rearrangement or the appearance of shear-induced structuring. For context, the maximum shear rate at the bottom of the channel is estimated by

$$\dot{\gamma} = \left(\frac{2n+1}{n}\right)\frac{Q}{bY^2}, \tag{1.1}$$

where Q is the volumetric flow rate, b the channel width, and Y the flow depth. In experiment 1, the minimum shear rate at the measurement section (Y_1) is approximately $650\,\mathrm{s}^{-1}$, with even higher values attained in subsequent experiments. This range is well above the observed discontinuity. Therefore, the discontinuity observed in the rheometric data occurs at shear rates significantly lower than those relevant to the flow conditions studied. Consequently, its effect on the interpretation of flow behaviour and model predictions within the experimental regime is negligible.

Density measurements were performed using an Anton Paar DMA5000 densimeter.

The geometry of the hydraulic jump was analyzed from video recordings captured at 25 frames per second with a resolution of 1920×1080 pixels. Although the shear-thinning and Newtonian fluids were sufficiently transparent to allow illumination from below, the shear-thickening fluid was opaque, necessitating an alternative visualization method. To this end, a grid was projected onto the fluid surface using an overhead projector. In the present experimental campaign, the velocity field was not measured, as the primary objective was the determination of the Mach angle β. Consequently, ensuring optical accessibility of the fluid for techniques such as Particle Image Velocimetry (PIV) or Laser Doppler Anemometry (LDA) was not required.

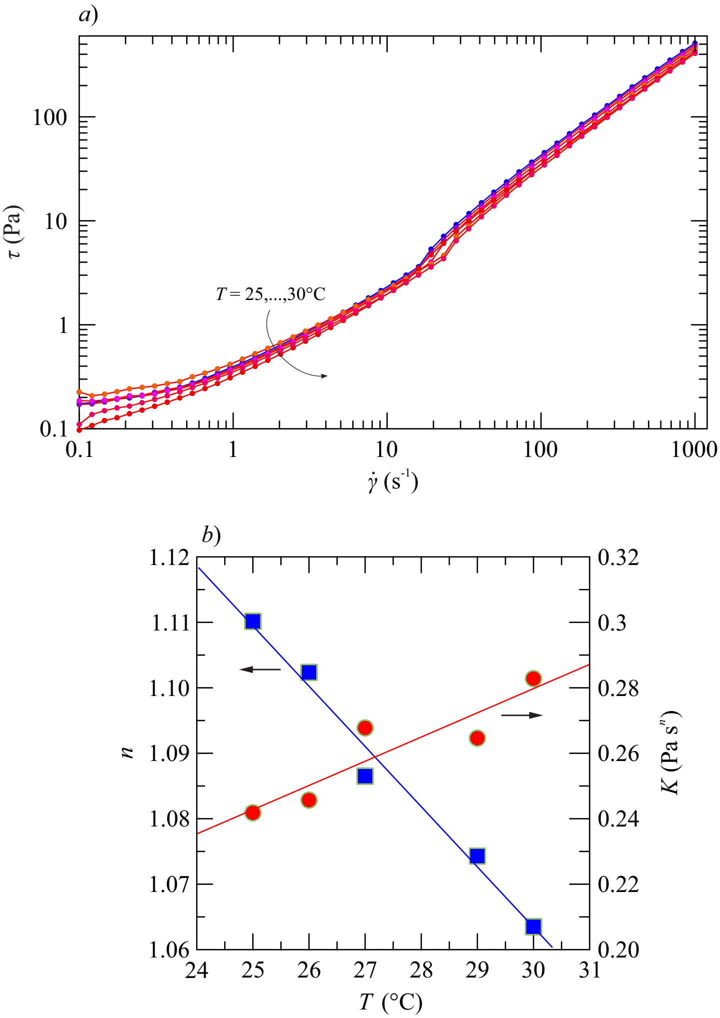

Figure 2: Shear-thickening fluid. (*a*) Experimental rheometric curves of shear stress versus shear rate at temperatures between 25 and 30 °C; (*b*) temperature dependence of the consistency index and fluid behaviour index.

2. Two-dimensional shallow-water model: numerical details

In the present section some details concerning the numerical solution of system (5.1)–(5.3), along with (5.4)–(5.5), are given.

Introducing the conservative variables

$$\mathbf{w} = \left(Y, q_x, q_y\right)^T = \left(Y, YV_x, YV_y\right)^T, \tag{2.1}$$

the conservation laws (5.1)–(5.3) can be recast in vector form:

$$\frac{\partial \mathbf{w}}{\partial t} + \frac{\partial \mathbf{f}}{\partial x} + \frac{\partial \mathbf{g}}{\partial y} = \mathbf{s}, \tag{2.2}$$

where the flux vectors **f** and **g** and the source term **s** are:

$$\mathbf{f} = \left(q_x, C_M \frac{q_x^2}{Y} + g\frac{Y^2}{2}, C_M \frac{q_x q_y}{Y}\right)^T, \tag{2.3}$$

Focus on Fluids articles must not exceed this page length

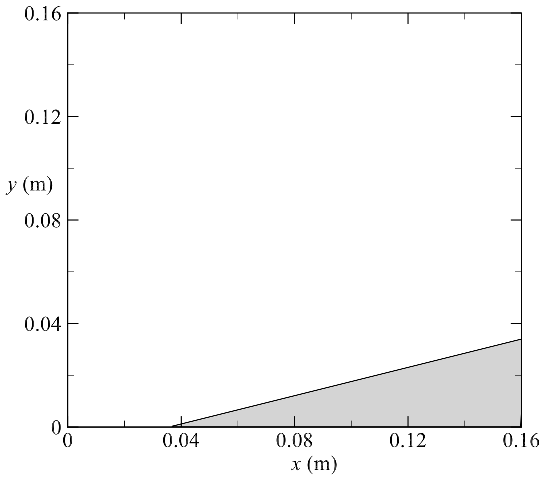

Figure 3: Schematic of the computational domain, with the wedge-shaped region of channel deflection ($\theta = 15°$) shaded in the bottom right.

$$\mathbf{g} = \left(q_y, C_M \frac{q_x q_y}{Y}, C_M \frac{q_y^2}{Y} + g\frac{Y^2}{2} \right)^T, \tag{2.4}$$

$$\mathbf{s} = \left(0, s_x, s_y\right)^T, \tag{2.5}$$

and the expressions of s_x and s_y directly follow from (5.4) and (5.5) accounting for (2.1). System (5.1)–(5.3) is hyperbolic, with eigenvalues of the flux Jacobian matrix $\mathbf{C} = n_x \mathbf{A} + n_y \mathbf{B}$ (where $\mathbf{A}$ and $\mathbf{B}$ are the Jacobians of $\mathbf{f}$ and $\mathbf{g}$ with respect to $\mathbf{w}$) expressed in primitive variables (Y, V_x, V_y) as

$$\lambda_1 = C_M\ \boldsymbol{V} \cdot \boldsymbol{n}, \qquad \lambda_{2,3} = C_M\ \boldsymbol{V} \cdot \boldsymbol{n} \pm \sqrt{C_M\left(C_M - 1\right)\left(\boldsymbol{V} \cdot \boldsymbol{n}\right)^2 + gY}, \tag{2.6}$$

where $\mathbf{n} = \left(n_x, n_y\right)^T$ denotes the unit vector of an arbitrary direction in the (x, y) plane.

System (2.2) is numerically solved using a cell-centred finite-volume method. Simulations were performed using a simplified square computational domain. A schematic of the domain for a deviation angle of $\theta = 15°$ is shown in Figure 3.

The computational domain is first discretized into a set of triangular cells forming an unstructured computational mesh. Denote by $\overline{\mathbf{w}}_i$ (respectively, $\overline{\mathbf{s}}_i$) the cell average values of $\mathbf{w}$ (respectively, $\mathbf{s}$) over the i-th triangular cell with area A_i. The integral form of equation (2.2) applied to each control volume reads (Anastasiou and Chan 1997):

$$\frac{\mathrm{d}}{\mathrm{dt}}\overline{\mathbf{w}}_i = -\frac{1}{A_i} \sum_{j=k(i)} \boldsymbol{F}_{i,j}^N l_j + \overline{\mathbf{s}}_i. \tag{2.7}$$

Here, $k(i)$ denotes the set of adjacent cells of cell i, l_j represents the length of the edge j, and $\mathbf{F}_{i,j}^N$ is the numerical flux across the interface between cells i and j. This flux provides a numerical approximation of $\mathbf{f}n_x + \mathbf{g}n_y$ across the edge j, where $\mathbf{n} = (n_x, n_y)^T$ is the outward normal vector to the j-th edge. For a cell-centered scheme on a triangular mesh, the set $k(i)$ contains exactly three neighbouring cells.

The morphodynamical solver developed by Evangelista et al. (2015) has been adapted here to simulate power-law fluids over a fixed bed. The numerical scheme used is first-order accurate in both space and time. The numerical fluxes, $\boldsymbol{F}^N$, are computed using the Harten–Lax–Van Leer (HLL) scheme (Harten et al. 1983), incorporating the eigenvalue expressions given in (2.6). The volume-averaged source term $\overline{\boldsymbol{s}}_i$ is evaluated based on pointwise approximation. The temporal integration of equation (2.7) is carried out using the explicit Euler forward finite-difference method.

3. Three-dimensional model

3.1. *Numerical details*

This section provides details about the numerical solution of the depth-resolved model. The solver `interFoam` was employed to integrate the continuity and momentum equations, incorporating a shear-dependent viscosity consistent with a power-law rheological model. In addition, an advection equation for the volume fraction of water, φ, was solved to capture the interface between the liquid and the surrounding air by means of the Volume-of-Fluid (VOF) method. The air phase was treated as an incompressible Newtonian fluid. The governing equations read:

$$\frac{\partial u_j}{\partial x_j} = 0, \tag{3.1}$$

$$\rho\frac{\partial u_i}{\partial t} + \rho\frac{\partial u_i u_j}{\partial x_j} = -\frac{\partial p}{\partial x_i} + \frac{\partial}{\partial x_j}\left[\mu\left(\frac{\partial u_i}{\partial x_j} + \frac{\partial u_j}{\partial x_i}\right)\right] - \rho b_i, \tag{3.2}$$

where p and u_i represent the pressure and the $i-$th Cartesian velocity component, respectively. In Eq. (3.2) x_1, x_2, x_3 denote the three spatial coordinates (with x_3 normal to the bottom) and b_i accounts for the weight force. The channel inclination has therefore been represented by a proper specification of the body force components b_1 and b_2.

According to the constitutive relation of a power-law fluid, the shear-dependent viscosity is:

$$\mu = k\ \left(S_{ij}S_{ij}\right)^{\frac{n-1}{2}}, \tag{3.3}$$

with S_{ij} the velocity deformation tensor:

$$S_{ij} = \frac{1}{2}\left(\frac{\partial u_i}{\partial x_j} + \frac{\partial u_j}{\partial x_i}\right). \tag{3.4}$$

The air–fluid interface is modeled using an algebraic VOF approach. A pure advection equation is solved for the volume fraction of water, φ, throughout the computational domain:

$$\frac{\partial \varphi}{\partial t} + u_j\frac{\partial \varphi}{\partial x_j} + u_j^r\frac{\partial \varphi(1-\varphi)}{\partial x_j} = 0. \tag{3.5}$$

In cells containing only water, $\varphi = 1$, whereas in cells containing only air $\varphi = 0$. In equation (3.5), $\mathbf{u}^r$ denotes the relative velocity of the fluid with respect to the air. Inclusion of this term enables for sharper resolution of the interface, as demonstrated by Berberovic (2009).

A combination of the PISO (Pressure Implicit with Splitting of Operators) and SIMPLE (Semi-Implicit Method for Pressure-Linked Equations) algorithms is employed to integrate the discretized equations, which are advanced in time using an implicit Euler scheme. Divergence terms are discretized using a blend of second-order linear interpolation together with the schemes of Warming and Beam (1976) and Van Leer (1974), whereas diffusive and pressure–gradient terms are approximated with a second-order linear scheme. The implicit Euler time discretization is first-order accurate.

Due to the non-linearity of both convective and diffusive terms, the equations are solved iteratively. The resulting linear systems are handled using a preconditioned conjugate gradient (PCG) method.

Figure 4(a) reports additional results of the numerical simulations with reference to Test 4 (shear-thinning fluid). The plot, in dimensionless coordinates and variables, represents a slice of the simulated flow field at $\hat{z} = 1$, which roughly corresponds to the flow depth at $\hat{x} = 0$, i.e., $\hat{Y}_1$. The streamlines of the tangent velocity $\hat{\mathbf{u}}_{xy} = \left(\hat{u}_x, \hat{u}_y, 0\right)$ are superimposed, along with a shaded contour level plot of the vertical velocity component $\hat{u}_z$. Considering that the dimensionless upstream velocity is $\hat{V}_1 \simeq 7$, Figure 4(a) shows that the horizontal component of the velocity exceeds the vertical component of more than one order of magnitude, supporting the validity of the shallow-water assumption. The vertical velocity component becomes relatively higher just upstream the front position predicted by the 1D models. Upon closer inspection the shape of this region of relatively higher values of $\hat{u}_z$ also appears to be slightly concave, in agreement with the behavior of $\hat{y}_F^{1\mathrm{D-S}}$. Interestingly, an appreciable deflection of the $\hat{\mathbf{u}}_{xy}$ velocity vector is apparent only in the region comprised between the $\hat{y}_F^{1\mathrm{D}}$ front and the deviated sidewall. Figures 4(c)-4(e) highlight the occurrence of three-dimensional flow structures in the vicinity of the deviated sidewall. Indeed, the shear exerted by the deviated sidewall induces a clockwise rotating corner vortex with a nearly triangular shape, and a counter-rotating one interacting with the free-surface. The vortex core, marked with a red circle in the figures, progressively moves upward and away from the sidewall. At the same time, the extension of corner vortex also increases from upstream to downstream. The marginal sensitivity of the free surface contour line to the computational mesh is also shown Figures 4(c)-4(e), confirming the quality of the present results. Finally, Figure 4(b) provides the mesh sensitivity of the vertical distribution of the three-dimensional velocity components for a representative alignment of the domain, corresponding to the location of the vortex core on the cross section at $\hat{x} = 20$. Figure 4(b) confirms the marginal mesh dependence of the results even in terms of velocity components.

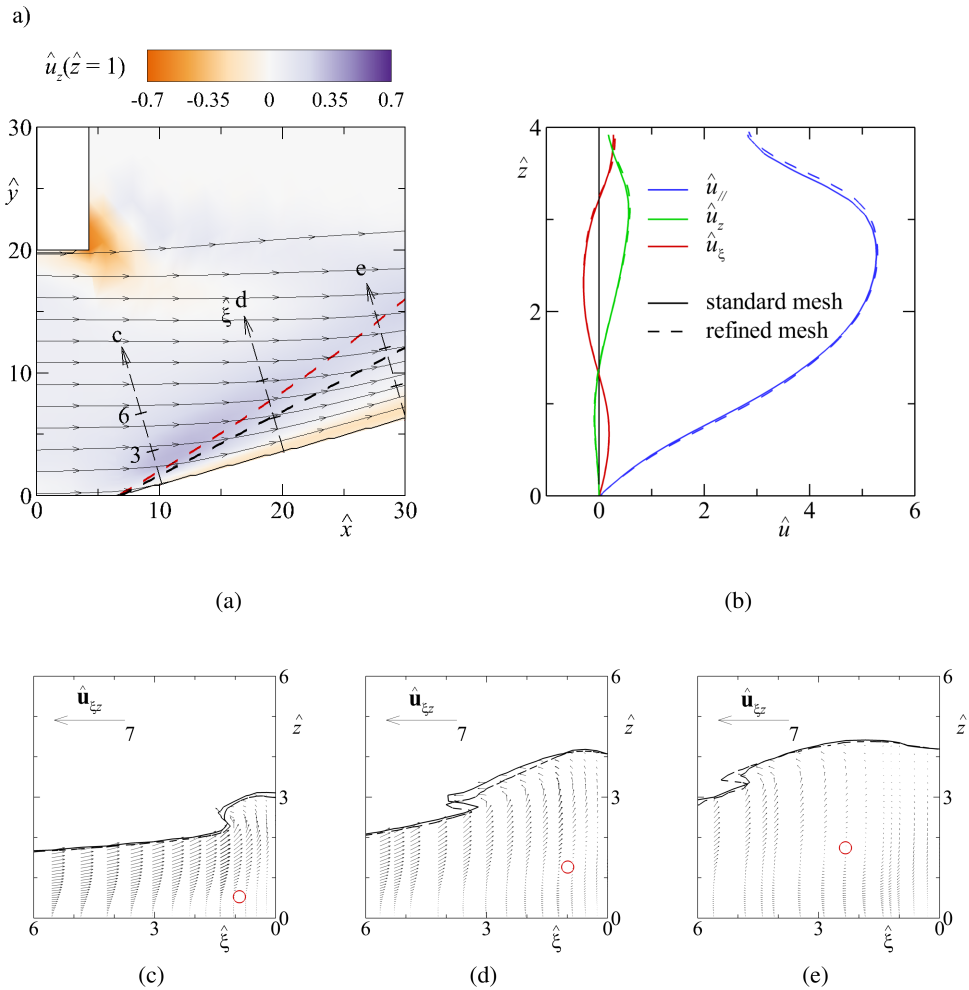

Figure 4: Test 4 (Shear-thinning fluid). (*a*). Streamlines of the tangent velocity and contour plot of dimensionless vertical velocity component $\hat{u}_z$ at $\hat{z} \simeq \hat{Y}_1$. Black dashed–line: $\hat{y}_F^{1\mathrm{D}}$. Red dashed–line: $\hat{y}_F^{1\mathrm{D-S}}$. (*b*) Mesh sensitivity of computed the velocity field in a representative point of the flow domain (cross section at $\hat{x} = 20$, $\hat{\xi} = 0.87$, red circle in panel d). (*c, d, e*) Velocity vector plot of tangent flow field $\hat{\mathbf{u}}_{\xi z}$ and $\varphi = 0.1$ line. Solid line: standard mesh. Dashed line: refined mesh.

REFERENCES

Anastasiou K. and Chan C. T. 1997 Solution of the 2D shallow water equations using the finite volume method on unstructured triangular meshes, *International Journal of Numerical Methods in Fluids*, **Vol. 24:11**, pp. 1225-1245.

Berberović, E., Hinsberg, N., Jakirlić, S., Roisman, I. and Tropea, C. 2009 Drop impact onto a liquid layer of finite thickness: Dynamics of the cavity evolution, *Phys. Rev. E*, **Vol. 79**, 036306.

Evangelista, S., Greco, M., Iervolino, M., Leopardi, A. and Vacca, A. 2015 A new algorithm for bank-failure machanism in 2D morphodynamic models with unbstructed grids, *International Journal of Sediment Research*, **Vol. 30:4**, pp. 382-391.

Harten, A., Lax, P. D. and van Leer, B. 1983 On Upstream Differencing and Godunov-Type Schemes for Hyperbolic Conservation Laws, *SIAM Review*, **Vol. 25:1**, pp.35–61.

Van Leer, B. 1974 Towards the ultimate conservative difference scheme. II. Monotonicity and conservation combined in a second-order scheme, *Journal Of Computational Physics*, **Vol. 14**, pp. 361-370.

Warming, R. and Beam, R. 1976 Upwind Second-Order Difference Schemes and Applications in Aerodynamic Flows., *AIAA Journal*, **Vol. 14**, pp. 1241-1249.